Simultaneous Cassini VIMS and UVIS observations of Saturn's southern aurora: Comparing emissions from H, H_2 and H_3^+ at a high spatial resolution

H. Melin,[1,2] T. Stallard,[1] S. Miller,[3] J. Gustin,[4] M. Galand,[5] S. V. Badman,[6] W. R. Pryor,[2,7] J. O'Donoghue,[1] R. H. Brown,[8] and K. H. Baines[9]

Received 8 June 2011; revised 30 June 2011; accepted 3 July 2011; published 10 August 2011.

[1] Here, for the first time, temporally coincident and spatially overlapping Cassini VIMS and UVIS observations of Saturn's southern aurora are presented. Ultraviolet auroral H and H_2 emissions from UVIS are compared to infrared H_3^+ emission from VIMS. The auroral emission is structured into three arcs – H, H_2 and H_3^+ are morphologically identical in the bright main auroral oval (~73°S), but there is an equatorward arc that is seen predominantly in H (~70°S), and a poleward arc (~74°S) that is seen mainly in H_2 and H_3^+. These observations indicate that, for the main auroral oval, UV emission is a good proxy for the infrared H_3^+ morphology (and vice versa), but for emission either poleward or equatorward this is no longer true. Hence, simultaneous UV/IR observations are crucial for completing the picture of how the atmosphere interacts with the magnetosphere.
Citation: Melin, H., T. Stallard, S. Miller, J. Gustin, M. Galand, S. V. Badman, W. R. Pryor, J. O'Donoghue, R. H. Brown, and K. H. Baines (2011), Simultaneous Cassini VIMS and UVIS observations of Saturn's southern aurora: Comparing emissions from H, H_2 and H_3^+ at a high spatial resolution, *Geophys. Res. Lett.*, *38*, L15203, doi:10.1029/2011GL048457.

1. Introduction

[2] The kronian aurora has been observed in the radio, infrared, visible, ultraviolet wavelengths (see overview by *Bhardwaj and Gladstone* [2000] and *Kurth et al.* [2009]). Whilst the planet's aurora has been extensively observed both in the infrared and the ultraviolet, no study has ever examined UV and IR observations that are both temporally and spatially simultaneous.

[3] *Cowley et al.* [2008] concluded that for a set of HST observations in the UV, the main auroral oval of Saturn was consistent with an open-closed boundary particle flux, caused by the shear between plasma moving at the solar-wind speed and the plasma confined inside the magnetosphere. Thus, emission poleward of the main auroral oval, located at a statistical average of ~73°S latitude in both the UV [*Badman et al.*, 2006; *Lamy et al.*, 2009] and the IR [*Badman et al.*, 2011], could be mapped to open field lines such that any excitation or ionisation of the atmosphere is caused by direct sourcing from the field-aligned component of the solar wind [*Clarke et al.*, 2005]. This picture is complicated, however, by evidence of both plasma convection inside the magnetosphere [*Hill et al.*, 2005], and in-situ observations of closed field line systems at high latitudes [*Mitchell et al.*, 2009].

[4] With Cassini, currently in orbit at Saturn, it is possible to observe Saturn's aurora with the Visual Infrared Mapping Spectrometer (VIMS) and the Ultraviolet Imaging Spectrograph (UVIS) simultaneously. Here, we start by briefly describing the characteristics and operational modes of the two instruments, examining what degree of temporal and spatial simultaneity can be achieved when operated in their respective standard modes, crucial for interpreting this dataset, before presenting our findings.

2. Cassini Observations

[5] The Cassini observations of Saturn's southern aurora presented here were obtained on 2008-254 (day of year – 10th of September). Cassini is at a distance of ~6 R_S from the centre of Saturn with a sub–spacecraft latitude of 75°S and a sub-solar latitude of 5°S. Whilst pointing at a fixed local time of 04:55 on the nightside pre-dawn sector of Saturn, VIMS and UVIS were both taking data for a duration of just over an hour. The spatial resolution on the body of Saturn for these observations is about 300 km per mrad, providing a partial view of the pre-dawn auroral region – the observational geometry is schematically shown in Figure 1, projected to longitude and planetocentric latitude.

2.1. UVIS Observations

[6] The UVIS FUV channel [*Esposito et al.*, 2004], which is used here, covers wavelengths between 112 and 191 nm at a spectral resolution of $R = \lambda/\Delta\lambda \sim 500$ with 1024 spectral resolution elements. There are 64 spatial pixels, each with a field-of-view (FOV) along the slit of 1 mrad, with a width of 1.5 mrad, using the low spectral resolution slit configuration.

[7] The UVIS observations started at 16:38 UT, finished at 17:42 UT and is comprised of 17 exposures each 240

[1]Department of Physics and Astronomy, University of Leicester, Leicester, UK.
[2]Space Environment Technologies, Los Angeles, California, USA.
[3]Department of Physics and Astronomy, University College London, London, UK.
[4]Institut d'Astrophysique et de Géophysique, University of Liege, Liege, Belgium.
[5]Department of Physics, Imperial College London, London, UK.
[6]Institute of Space and Astronautical Science, JAXA, Sagamihara, Japan.
[7]Central Arizona College, Coolidge, Arizona, USA.
[8]Department of Planetary Sciences, University of Arizona, Tucson, Arizona, USA.
[9]Jet Propulsion Laboratory, California Institute of Technology, Pasadena, California, USA.

0094-8276/11/2011GL048457

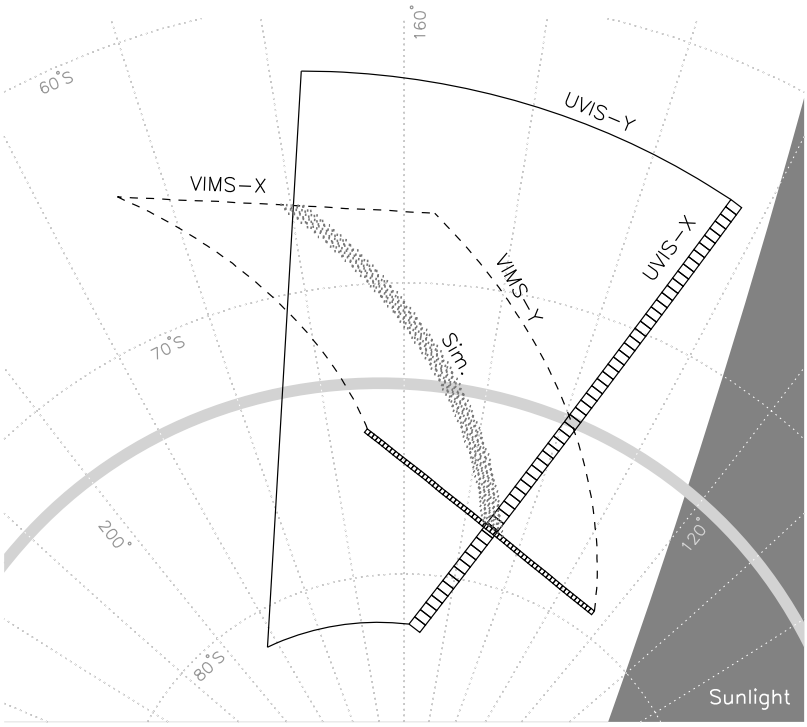

Figure 1. Schematic showing the UVIS (solid line) and VIMS (dashed line) latitude-longitude projected field of view, with the swath of simultaneity (dotted area, labelled 'Sim.'). The grid has as spacing of 10° in both latitude and longitude, with the south pole towards the bottom. Individual pixel projections are shown at the starting point of each instrument FOV. The light grey semicircle shows the average location of the southern auroral oval [*Badman et al.*, 2011a]. The dark grey area to the right shows the sunlight at the start of the observation.

seconds long with the centre of the UVIS slit pointing at a constant 04:55 LT. The data is calibrated using the pipeline developed at LASP at the University of Colorado.

[8] The latitude-longitude projected UVIS FOV for this set of observations can be seen in Figure 1 (solid line). The 64 spatial pixels of a single exposure are aligned along UVIS-X (each pixel shown), such that subsequent exposures are located westward along UVIS-Y (leftward in Figure 1) describing the temporal evolution during the 17 exposures at the fixed local time of the UVIS slit. Note that if projected to latitude and local time, all of the UVIS observations would stack atop each other.

[9] Here, we analyse emission from molecular hydrogen, by integrating across H Lyman-α at 122 nm (hereafter H), and molecular hydrogen, by summing the H_2 Lyman and Werner bands between 123 nm and 166 nm (hereafter H_2).

2.2. VIMS Observations

[10] VIMS is a visual and infrared imaging spectrograph [*Brown et al.*, 2004] with a field of view of 32 × 32 mrad, divided into 64 × 64 spatial pixels, each covering 0.5 mrad square. Each spatial pixel has 256 spectral pixels covering 0.8 μm to 5.1 μm at a spectral resolution of $R = \lambda/\Delta\lambda \sim 200$. Pixels are integrated in sequence by moving an internal mirror in a 'whiskbroom' fashion, such that a single VIMS data cube is comprised of 4,160 single exposures (64 × 64 pixels + 64 background pixels that quantify the thermal noise).

[11] The latitude-longitude projected VIMS FOV can be seen in Figure 1 (dashed line). The first line of pixels are indicated along VIMS-X, with each line being integrated from right to left. At each subsequent VIMS-Y position the instrument scans along VIMS-X.

[12] The VIMS integration started at 16:34 UT and the last pixel was integrated at 17:42 UT, comprising of a complete 64 × 64 × 256 spectral cube, each pixel having an integration time of 1 s.

[13] Here, VIMS bins 250 (3.41 μm), 252 (3.45 μm), 257 (3.53 μm), 262 (3.61 μm) and 265 (3.67 μm) are used which all contain H_3^+ R branch emission, with each bin having a width of 0.017 μm. The VIMS data is processed through the standard pipeline developed at the University of Arizona, and is subject to a partial background subtraction to remove instrumental artefacts.

2.3. Simultaneous VIMS and UVIS Operation

[14] Both instruments are mounted on Cassini's Remote Sensing Palette (RSP), with boresights pointing along the −Y direction in space-craft coordinate system, with −Z pointing along the high-gain antenna. Only 4.6% of the VIMS FOV overlaps spatially with the UVIS slit. Since the exposure times per pixel are here 240 times greater for UVIS than VIMS (1 s for VIMS and 240 s for UVIS), and with 6 VIMS pixels subtending an angular area equal to one UVIS pixel, we expect that these observations are only temporally simultaneous 2.5% of the total exposure time. Thus, the combined true spatial and temporal simultaneity between the two instruments for this set of observations is dwindlingly small (0.1%). Instead, we consider the it *swath of simultaneity* that is defined by VIMS and UVIS pixels that are at some (any) point both temporally and spatially

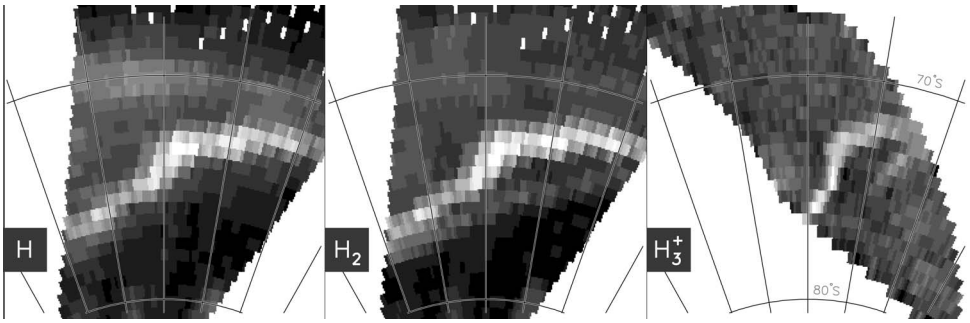

Figure 2. The latitude-longitude projected Cassini VIMS and UVIS observations of 2008-254 showing ultraviolet H Lyman-α, H_2 Lyman band emission and near-infrared H_3^+ emission. The geometry is described in Figure 1 – note that only a very small part of these observations are both temporally and spatially simultaneous.

overlapping, regardless of how small this overlap may be – this can be seen in Figure 1 (dotted area).

3. Results

[15] The UVIS (H and H_2) and VIMS (H_3^+) observations can be seen in Figure 2, projected to latitude-longitude, with the projection geometry being the same as that of Figure 1. All observations are projected to an altitude of 1100 km above the 1 bar level [*Gérard et al.*, 2009], and are mapped onto a 0.5° × 0.5° grid.

[16] The H plot in Figure 2 shows a bright main arc that rotates into the UVIS FOV, appearing to move poleward from 73°S to 77°S at the fixed local time of the slit (hereafter referred to as the main arc). The peak H brightness is 1.6 kR with the brightness varying by as much as 20% between exposures. There is also a broad equatorward diffuse arc at 70°S that brightens by ~20% over the course of these observations, with a peak brightness of 0.6 kR.

[17] The H_2 plot in Figure 2 shows both the main arc (peak brightness 3.8 kR) and the equatorial arc (peak brightness 0.8 kR) identified in H, but displays larger variations – up to 40% between individual UVIS exposures. There is also another distinct third arc, seen ~1° poleward of the main arc, moving alongside it with the distance between the arcs decreasing with time. Note that due to the very broad line spread function of the FUV instrument, there is likely some contamination from H Lyman-α in the region long-ward of 122 nm.

[18] The H_3^+ plot in Figure 2 shows the main arc already seen in H and H_2, and a poleward arc extending only through half of the VIMS FOV.

[19] Figure 3 shows the brightness of H, H_2 and H_3^+ along the swath of simultaneity (shown in Figure 1). These emissions are simultaneous both temporally and spatially within a time scale of 240 seconds. The difference between the species already seen in Figure 2 are clearly evident. Given the H_3^+ error bar and the possible H contamination of H_2 it is unclear if the equatorward arc exists in these species. Similarly, the poleward arc may be present in H, but may be masked by the apparent broadening of the intensity distribution compared to H_2.

3.1. Physical Properties of H_3^+

[20] Modelling the H_3^+ emission as observed through the VIMS spectral bins using the spectral data of *Neale et al.*

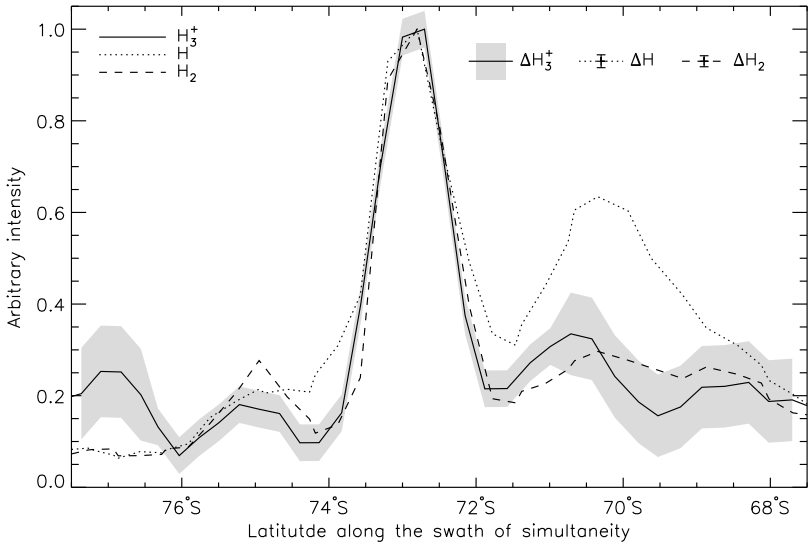

Figure 3. The intensity profile along the swath of simultaneity (shown in Figure 1) of H Lyman-α (dotted line), H_2 Lyman bands (dashed line) and H_3^+ (solid line). The shaded area shows the error on the H_3^+ intensity, with the error on H and H_2 indicated by respective error bars. The varying H_3^+ error is associated with the background subtraction process.

Table 1. The Parameters Derived for the Arcs Seen in the Simultaneous VIMS (H_3^+) and UVIS (H and H_2) Observations of 2008-254 16:30 of Saturn's Southern Aurora

Parameter	Equatorward	Main	Poleward
Latitude	70°S	73°S	74°S
Arc FWHM (°latitude)	2.0	1.5	1.2
FUV intensity (kR)	2.1	5.0	1.6
Precipitation energy (mWm^{-2})	0.33	0.80	0.25
H_3^+ temperature (K)	–	440 ± 50	–
H_3^+ density (10^{15} m^{-2})	–	7 ± 1	–
H_3^+ cooling (mWm^{-2})	–	0.4	–

[1996] and assuming conditions of q-LTE [*Miller et al.*, 1990], we analyse the temperature dependence of the following ratio:

$$b = \frac{I_{3.41}^{250} + I_{3.44}^{252} + I_{3.53}^{257}}{I_{3.61}^{262} + I_{3.67}^{265}} \quad (1)$$

where I is the intensity contained within a particular spectral pixel – the superscript denotes the VIMS wavelength bin number (from the start of short visible wavelengths) and the subscript is the centre of the wavelength bin in μm with each bin having a width of 0.017 μm. The relationship between effective H_3^+ temperature, T, and the intensity ratio b in equation (1) is given by:

$$T(b) = 122 + 289b - 62b^2 + 25b^3 \quad (2)$$

[21] The VIMS spectral bins that contain the H_3^+ R branch emission at around 3.5 μm have relatively little additional emission from other species within them, and is a region that is not significantly affected by sunlight, as opposed to both the Q and the P branch emissions at longer wavelengths. Here, we make a first order assumption and subtract off a constant background for each bin for all the terms of equation (1), before calculating the ratio. Very small changes in the background subtraction can have large effects on the derived temperature.

[22] The mean temperature along the main auroral arc is derived to be T = 440 ± 50 K. Given that temperature and a total flux of the numerator in equation (1) of 1.8 × 10^{-7} $Wm^{-2}str^{-1}$, the column integrated density is 7 ± 1 × 10^{15} m^{-2} and the total energy emitted by the H_3^+ column is 0.4 mWm^{-2}. The temperature derived here is comparable to the values measured using ground-based observations by *Melin et al.* [2007] (390 ± 70 K and 420 ± 70 K) and to those derived in the UV by *Gustin et al.* [2009] (400 K and 500 K with FUSE).

3.2. Precipitation Energies

[23] For each of the three arcs the UVIS FUV spectrum was extracted and compared to a 100 eV and 20 eV monoenergetic H_2 laboratory spectrum, giving the energy of the electron population responsible for exciting the H_2 (see *Gustin et al.* [2009] for details). Both the equatorward and the poleward arc compares better to the 20 eV H_2 spectrum whereas the main arc compares better to the 100 eV H_2 spectrum. None of the FUV arc spectra show any evidence of hydrocarbon absorption, suggesting that the precipitation energies required to produce the observed arcs cannot be larger than a few keV [*Gustin et al.*, 2009] as not to excite/ionise H and H_2 close to the homopause, where hydrocarbons are prevalent. Note that H contamination at H_2 band wavelengths has little effect on the spectral shape that enables this analysis.

[24] Using the conversion rate of 0.16 mWm^{-2} of precipitation energy flux per 1 kR of FUV emission of *Grodent et al.* [2010], we can derive the required energy to produce each of the three arcs observed here. These are 0.33, 0.80 and 0.25 mWm^{-2} for the equatorward, main and poleward arcs respectively.

4. Discussion

[25] The various derived physical properties for the observed three arcs can be seen in Table 1.

[26] The average position of the main arc seen in all three species agrees well with the statistical ovals at 73°S latitude of *Badman et al.* [2006] and S. V. Badman (Cassini VIMS observations of latitudinal and hemisphericvariations in Saturn's infrared auroral intensity, submitted to *Icarus*, 2011), generally thought to be associated with the open-closed field line boundary [*Bunce et al.*, 2008]. With the precipitation energy limit of a few keV's, the energy distribution must be broad as to excite and ionize throughout the upper atmosphere.

[27] Figure 3 shows that the H intensity profile having broader wings than both H_2 and H_3^+, indicative of softer precipitation energies at the boundaries of the auroral current that produce the main auroral arc.

[28] The diffuse arc seen predominantly in H requires the precipitation energy to be deposited at high altitudes. This precludes hard precipitation, with the primary energy being on the order of 100s of eV [*Gustin et al.*, 2009]. This arc is poleward of the diffuse emission observed by *Grodent et al.* [2010] at 67°S with an energy of 0.3 mWm^{-2}, which is the same as the 0.33 mWm^{-2} seen here. This arc is also poleward of the auroral emission associated with the breakdown of co-rotation close to Enceladus at ~55°S [*Stallard et al.*, 2010]. Given the low energy of the precipitation and the width of the distribution, there is also the possibility of this being proton aurora [e.g., *Iglesias and Vondrak*, 1974].

[29] The poleward arc seen in H_2 and H_3^+ (and possibly H) presents a greater challenge – if the main arc is associated with the open/closed field line boundary, then this arc is connected to the solar wind via the open field lines. However, given the high spatial resolution of these observations, we could be seeing the return flow of the open-closed boundary current system, responsible for the main auroral arc [see *Talboys et al.*, 2009]. On the other hand, the poleward arc only extends across half the VIMS FOV, whilst it is visible throughout the UVIS observations. There is no direct observational evidence that this arc exists at local times earlier than the position of the UVIS slit and thus the poleward arc may indeed be forming at 04:55 LT, extending towards dawn. If this region is magnetically connected to the solar wind, this arc could be produced by a local plasma enhancement of the solar wind. However, since the precipitation energy is required to be hard (few keV) as to penetrate deep into the atmosphere to excite and ionize H_2, direct sourcing from the solar wind seems unlikely.

[30] Using the STIM model *Galand et al.* [2011] derived an auroral electron density of ~2 × 10^9 m^{-3} and an H_2 density of ~10^{17} m^{-3} at 1100 km above the 1 bar level (10^{-5} bar). The fraction of H_2 molecules with sufficient thermal energy to collisionally excite H_3^+ to its first vibrational level,

ν_2, at 440 K is about one in 10,000, assuming conditions of q-LTE. Given this ratio and a proton hopping rate of 2×10^{-15} m^{-3} [*Theard and Huntress*, 1974], the collisional excitation time is 26 seconds. The lifetime, using the recombination constant of *Leu et al.* [1973], is about 500 seconds, twice the length of a UVIS exposure. This is consistent with what is observed here, since the H_3^+ follows the morphology of both H and H_2 in the main arc – the H_3^+ emission would be trailing if its lifetime was considerably longer. In addition, given that the collisional population time is considerably shorter than the lifetime of the molecule, the assumption of q-LTE appears valid.

5. Conclusions

[31] We have presented high resolution simultaneous Cassini VIMS and UVIS observations of Saturn's southern aurora. Three very different arcs are observed, likely caused by different particle precipitation energies, depositing energy at different altitudes. These observations highlight the very dynamic behaviour of the kronian aurora, with both complex small-scale structures and variability over short time-scales, and may serve as context for models detailing both the origin and atmospheric interaction of the particle precipitation.

[32] Despite the absence of a global view, these observations paint a similar picture to the simultaneous observations of Jupiter of *Clarke et al.* [2004], showing a good agreement between IR and UV when it comes to the main auroral oval, but there are significant differences both poleward and equatorward. Consequently one cannot assume that auroral morphology in the UV and IR is identical, with the exception of the main oval itself.

[33] **Acknowledgments.** This work was supported at the University of Leicester by the Science and Technology Facilities Council (STFC) grant PP/E/000983/1 and ST/G0022223/1 for H.M. and T.S., and a RCUK Fellowship for T.S. Supported at SET by NASA CDAP grant NNX10AG35G. M.G. was partially supported by the STFC rolling grant to Imperial College. We thank G. Holeslaw at LASP for supplying the UVIS calibration routines.

[34] The Editor thanks Anil Bhardwaj and an anonymous reviewer for their assistance in evaluating this paper.

References

Badman, S. V., S. W. H. Cowley, J. Gérard, and D. Grodent (2006), A statistical analysis of the location and width of Saturn's southern auroras, *Ann. Geophys.*, *24*, 3533–3545, doi:10.5194/angeo-24-3533-2006.

Badman, S. V., N. Achilleos, K. H. Baines, R. H. Brown, E. J. Bunce, M. K. Dougherty, H. Melin, J. D. Nichols, and T. Stallard (2011), Location of Saturn's northern infrared aurora determined from Cassini VIMS images, *Geophys. Res. Lett.*, *38*, L03102, doi:10.1029/2010GL046193.

Bhardwaj, A., and G. R. Gladstone (2000), Auroral emissions of the giant planets, *Rev. Geophys.*, *38*, 295–354, doi:10.1029/1998RG000046.

Brown, R. H., et al. (2004), The Cassini visual and infrared mapping spectrometer (VIMS) investigation, *Space Sci. Rev.*, *115*, 111–168, doi:10.1007/s11214-004-1453-x.

Bunce, E. J., et al. (2008), Origin of Saturn's aurora: Simultaneous observations by Cassini and the Hubble Space Telescope, *J. Geophys. Res.*, *113*, A09209, doi:10.1029/2008JA013257.

Clarke, J. T., D. Grodent, S. W. H. Cowley, E. J. Bunce, P. Zarka, J. E. P. Connerney, and T. Satoh (2004), Jupiter's aurora, in *Jupiter. The Planet, Satellites and Magnetosphere*, pp. 639–670, Cambridge Univ. Press, Cambridge, U. K.

Clarke, J. T., et al. (2005), Morphological differences between Saturn's ultraviolet aurorae and those of Earth and Jupiter, *Nature*, *433*, 717–719, doi:10.1038/nature03331.

Cowley, S. W. H., et al. (2008), Auroral current systems in Saturn's magnetosphere: comparison of theoretical models with Cassini and HST observations, *Ann. Geophys.*, *26*, 2613–2630, doi:10.5194/angeo-26-2613-2008.

Esposito, L. W., et al. (2004), The Cassini Ultraviolet Imaging Spectrograph investigation, *Space Sci. Rev.*, *115*, 299–361, doi:10.1007/s11214-004-1455-8.

Galand, M., L. Moore, I. Müller-Wodarg, M. Mendillo, and S. Miller (2011), Response of Saturn's auroral ionosphere to electron precipitation: electron density, electron temperature, and electrical conductivity, *J. Geophys. Res.*, doi:10.1029/2010JA016412, in press.

Gérard, J., B. Bonfond, J. Gustin, D. Grodent, J. T. Clarke, D. Bisikalo, and V. Shematovich (2009), Altitude of Saturn's aurora and its implications for the characteristic energy of precipitated electrons, *Geophys. Res. Lett.*, *36*, L02202, doi:10.1029/2008GL036554.

Grodent, D., A. Radioti, B. Bonfond, and J. Gérard (2010), On the origin of Saturn's outer auroral emission, *J. Geophys. Res.*, *115*, A08219, doi:10.1029/2009JA014901.

Gustin, J., J. Gérard, W. Pryor, P. D. Feldman, D. Grodent, and G. Holsclaw (2009), Characteristics of Saturn's polar atmosphere and auroral electrons derived from HST/STIS, FUSE and Cassini/UVIS spectra, *Icarus*, *200*, 176–187, doi:10.1016/j.icarus.2008.11.013.

Hill, T. W., et al. (2005), Evidence for rotationally driven plasma transport in Saturn's magnetosphere, *Geophys. Res. Lett.*, *32*, L14S10, doi:10.1029/2005GL022620.

Iglesias, G. E., and R. R. Vondrak (1974), Atmospheric spreading of protons in auroral arcs, *J. Geophys. Res.*, *79*, 280–282, doi:10.1029/JA079i001p00280.

Kurth, W. S., et al. (2009), Auroral processes, in *Saturn From Cassini-Huygens*, p. 333, Springer, New York.

Lamy, L., B. Cecconi, R. Prangé, P. Zarka, J. D. Nichols, and J. T. Clarke (2009), An auroral oval at the footprint of Saturn's kilometric radio sources, colocated with the UV aurorae, *J. Geophys. Res.*, *114*, A10212, doi:10.1029/2009JA014401.

Leu, M. T., M. A. Biondi, and R. Johnsen (1973), Measurements of recombination of electrons with H_3^+ and H_5^+ ions, *Physi. Rev. A*, *8*, 413–419, doi:10.1103/PhysRevA.8.413.

Melin, H., S. Miller, T. Stallard, L. M. Trafton, and T. R. Geballe (2007), Variability in the H_3^+ emission of Saturn: Consequences for ionisation rates and temperature, *Icarus*, *186*, 234–241, doi:10.1016/j.icarus.2006.08.014.

Miller, S., R. D. Joseph, and J. Tennyson (1990), Infrared emissions of H_3^+ in the atmosphere of Jupiter in the 2.1 and 4.0 micron region, *Astrophys. J.*, *360*, L55–L58, doi:10.1086/185811.

Mitchell, D. G., W. S. Kurth, G. B. Hospodarsky, N. Krupp, J. Saur, B. H. Mauk, J. F. Carbary, S. M. Krimigis, M. K. Dougherty, and D. C. Hamilton (2009), Ion conics and electron beams associated with auroral processes on Saturn, *J. Geophys. Res.*, *114*, A02212, doi:10.1029/2008JA013621.

Neale, L., S. Miller, and J. Tennyson (1996), Spectroscopic properties of the H_3^+ molecule: A new calculated line list, *Astrophys. J.*, *464*, 516–520, doi:10.1086/177341.

Stallard, T., H. Melin, S. W. H. Cowley, S. Miller, and M. B. Lystrup (2010), Location and magnetospheric mapping of Saturn's mid-latitude infrared auroral oval, *Astrophys. J.*, *722*, L85–L89, doi:10.1088/2041-8205/722/1/L85.

Talboys, D. L., C. S. Arridge, E. J. Bunce, A. J. Coates, S. W. H. Cowley, and M. K. Dougherty (2009), Characterization of auroral current systems in Saturn's magnetosphere: High-latitude Cassini observations, *J. Geophys. Res.*, *114*, A06220, doi:10.1029/2008JA013846.

Theard, L. P., and W. T. Huntress (1974), Ion-molecule reactions and vibrational deactivation of H_2^+ ions in mixtures of hydrogen and helium, *J. Chem. Phys.*, *60*, 2840–2848, doi:10.1063/1.1681453.

S. V. Badman, Institute of Space and Astronautical Science, JAXA, 3-1-1 Yoshinodai, Chuo-ku, Sagamihara, Kanagawa 252-5210, Japan. (s.badman@stp.isas.jaxa.jp)

K. H. Baines, Jet Propulsion Laboratory, California Institute of Technology, 4800 Oak Grove Dr., Pasadena, CA 91109, USA. (kbaines@scn.jpl.nasa.gov)

R. H. Brown, Department of Planetary Sciences, University of Arizona, Tucson, AZ 85721, USA.

M. Galand, Department of Physics, Imperial College London, Prince Consort Road, London SW7 2AZ, UK. (m.galand@imperial.ac.uk)

J. Gustin, Institut d'Astrophysique et de Géophysique, University of Liege, Liege B-4000, Belgium. (gustin@astro.ulg.ac.be)

H. Melin, J. O'Donoghue, and T. Stallard, Department of Physics and Astronomy, University of Leicester, University Road, Leicester LE1 7RH, UK. (h.melin@ion.le.ac.uk; jod3@ion.le.ac.uk; tss@ion.le.ac.uk)

S. Miller, Department of Physics and Astronomy, University College London, London WC1 6BT, UK. (s.miller@ucl.ac.uk)

W. R. Pryor, Central Arizona College, 8470 N. Overfield Rd., Coolidge, AZ 85228, USA. (wayne.pryor@centralaz.edu)